Nanomechanics and morphology of simulated respiratory particles

Robert Groth[1], Sadegh Niazi[1], Graham R. Johnson[1], and Zoran Ristovski[1*]

[1] International Laboratory for Air Quality and Health (ILAQH), School of Earth and Atmospheric Sciences, Queensland University of Technology, Brisbane, Australia

* Corresponding author: Zoran Ristovski, z.ristovski@qut.edu.au

Abstract

The impact of respiratory particle composition on the equilibrium morphology and phase are not well understood. Furthermore, the effects of these different phases and morphologies on the viability of viruses embedded within these particles are equally unknown. Physiologically relevant respiratory fluid analogues were constructed, and their hygroscopic behavior were measured using an ensemble technique. A relationship between hygroscopicity and protein concentration was determined, providing additional validation to the high protein content of respiratory aerosol measured in prior works (>90%). It was found that the salt component of the respiratory particles could crystallize as a single crystal, multiple crystals, or would not crystallize at all. It was found that dried protein particles at indoor-relevant climatic conditions could exist separately in a glassy (~77% of particles) or viscoelastic state (~23% of particles). The phase state and morphology of respiratory particles may influence the viability of embedded pathogens. We recommend that pathogen research aiming to mimic the native composition of respiratory fluid should use a protein concentration of at least 90% by solute volume to improve the representativity of the pathogen's microenvironment.

Keywords

respiratory aerosol, droplet physicochemistry, virus viability, glassy aerosol, hygroscopic growth, atomic force microscopy, transmission electron microscopy

Synopsis
We establish links between chemical and physical properties of simulated respiratory fluid. This work helps to explain the results of prior airborne virology studies and encourages scientists to use protein-enriched growth media for future work to accurately mimic human respiratory fluid.

1. Introduction

The emergence of the severe acute respiratory syndrome coronavirus 2 (SARS-CoV-2) pandemic has brought increased attention to the airborne transmission of viruses. There is evidence that the transmission of SARS-CoV-2, among other prominent respiratory viruses such as influenza and rhinovirus, can be through the airborne mode [1–3]. Recent research has solidified the importance of the airborne route and have highlighted the gaps in knowledge regarding this process [3–5]. Most importantly, the link between droplet physicochemistry and virus viability and transport are not well understood and yet are crucial for managing and preventing transmission. In measurements of airborne virus viability, climatic conditions, particularly absolute or relative humidity (RH) and temperature, have shown to be important factors in contribution to virus viability [6–12]. This is likely due to physical and chemical interactions between the ambient air and the particle in which the viruses are embedded [13].

Viruses emitted into the air through expiration (talking, breathing, coughing, sneezing, etc.) will be embedded in droplets composed of the fluid which lines the respiratory tract [14–16]. The solutes in this respiratory fluid will interact with the atmosphere and provide the microenvironment for the viruses. The exact composition and size of the respiratory aerosols can vary by production region and also between individuals [14,15,17,18]. The primary composition of respiratory fluid is proteins, inorganic salts and surfactants [19–21]. Simulating respiratory fluid for use in virus experiments is not trivial, as respiratory fluid is a viscoelastic fluid (e.g., mucus) and is not easily nebulized. The protein content of human respiratory aerosol is estimated to be upwards of 90% by solute total volume [17,22,23]. The primary inorganic is NaCl, which is a hygroscopic salt, and therefore human respiratory aerosol exhibits hygroscopic growth [17]. In the context of airborne virus transmission, this means that as the droplets are released into the atmosphere, they will release water to reach equilibrium with ambient RH. Additionally, the respiratory particles may exhibit RH-dependent discontinuous phase transitions depending on composition [17]. Upon dehydration, aqueous NaCl particles will promptly release the remaining liquid water and crystallize (effloresce) below the efflorescence RH (ERH, ~45% RH). Conversely, upon subsequent hydration, crystalline NaCl particles will uptake water vapor until prompt redissolution (deliquescence) at the deliquescence RH (DRH, ~75% RH). Deliquescence and efflorescence have also been observed in human respiratory aerosol, indicating that the phase state of the particles may have further influence on the viability of airborne viruses [17].

Studying the dynamics and viability of airborne viruses has been of importance in determining the transmission route of viral respiratory infections. Studies have been conducted on both infectious human respiratory viruses (influenza [6,9,24], SARS-CoV [25], rhinovirus [8]) and also on bacteriophages as viral surrogates (bacteriophage phi6 [26,27], MS2 [27,28]). The results of these studies suggest complex mechanisms determine the viability of the virus, with a 'V-shape' RH dependence being a common

66 occurrence for viruses nebulized in culture media. Increased fractions of viable viruses are observed at
67 high and low RH and viability is typically minimised at intermediate RH, while the effects of protein-
68 enriched media are inconclusive.

69 Effects of particle composition, morphology and phase state on virus viability are not well
70 understood, although it is clear that they are important. Phase transitions of hygroscopic salts may
71 explain parts of the V-shaped viability curve [8], and phase separated liquids may contribute to
72 inactivation at intermediate RH [29]. Semisolid phases, such as glassy or high viscosity semisolids, may
73 also influence virus viability at indoor-relevant RH [29–32]. Glassy aerosol are extremely viscous
74 semisolid particles and have bulk properties like solids (hardness, rigidity) and inhibit molecular
75 diffusion. The occurrence of these phenomena, of course, depend primarily on the interactions
76 between the particle solutes and the ambient atmosphere. If the primary mechanism of virus
77 inactivation in respiratory particles is through exposure to highly ionic solutions, such as concentrated
78 aqueous salts, then it becomes clear that higher protein concentration particles would favor virus
79 viability. Therefore, in laboratory studies of virus viability, it becomes most prudent to ensure that the
80 composition of the nebulization fluid is representative of typical respiratory aerosol. Studies have
81 aimed to use simulated respiratory fluid (SRF) to investigate aerosol dynamics and virus viability
82 [8,9,18,27,33,34]. In all cases, the primary components of the SRF were NaCl and protein (combinations of
83 mucins and albumins). It has been demonstrated that the composition of human respiratory aerosol
84 can be primarily proteins (>90% by volume) and may be useful in future works to incorporate larger
85 protein concentrations [17,29].

86 In this work, we investigate the effects of protein concentration on the morphology and phase state of
87 simulated respiratory particles. To clarify terminology for further reading, "aerosol" refers to particles
88 suspended in a gas and "droplet" refers to liquid aerosol particles. We use different particle protein
89 volume fractions and used an ensemble technique to measure the average hygroscopic behavior of the
90 particles at different RH values [17,35–37]. We collected particles for transmission electron microscopy
91 (TEM) and atomic force microscopy (AFM) analysis to determine morphology and viscoelastic
92 properties of the particles. Previous methods [38] were adapted to produce a phase diagram of SRF
93 aerosol as a function of RH, which predicts glassy solid phase of respiratory aerosol. The recent work
94 of Huynh et al. is supported in this work, identifying semisolid phases of SRF [29]. Particularly,
95 evidence of distinct viscoelastic semisolid phases of porcine gastric mucin were observed, varying
96 between glassy and moderately viscous. The influence of particle phase and morphology on virus
97 viability are not well understood, but the work here provides some foundation for future studies.

2. Materials and methods

2.1. Sample preparation

The bulk simulated respiratory fluid (SRF) mixtures used in this study were composed of water, porcine gastric mucin (PGM) (type III, Sigma-Aldrich) and NaCl (>99%, Sigma-Aldrich). PGM was used as an analogue for human respiratory mucin, as mucin 5AC are primary mucins present in both human airways and in the gastrointestinal tract of pigs [39,40]. Each mixture was prepared with a predetermined target organic mass fraction of dry solutes (w_O). The mass of the dry solutes were measured in separate vials and then added to 40 mL of 18.2 MΩ·cm water (Milli-Q). The final mass of the vials were then measured to calculate the organic volume fraction of dry solutes (ϕ_O) in each mixture (Table 1). The particles were generated using a Collison nebulizer with filtered and dried compressed air as the carrier gas.

Figure 1 panel	w_O	ϕ_O
(a)	0.238±0.004	0.385±0.01
(b)	0.538±0.005	0.700±0.01
(c)	0.666±0.007	0.800±0.02
(d)	0.741±0.007	0.851±0.02
(e)	0.811±0.01	0.896±0.02
(f)	0.905±0.02	0.950±0.05
(g)	0.912±0.02	0.954±0.05
(h)	0.934±0.03	0.966±0.06
(i)	1	1
(i)	1	1

Table 1. The measured organic mass fraction of dry solutes (w_O) and organic volume fraction of dry solutes (ϕ_O) in each simulated respiratory fluid solution.

Additionally, a solution of sucrose (>99.5%, Sigma-Aldrich) was used for force-response atomic force microscopy (AFM) analysis as representative of semisolid particles.

2.2. Hygroscopic growth measurements

The aerosol were passed through a silica diffusion dryer with an internal mesh (inner diameter = 2.5 cm) at 0.3 Lmin^{-1} for a total length of 80 cm (residence time ~80 s). The relative humidity (RH) after drying the particles was measured using a RH sensor (HC2-C04, Rotronic AG, Switzerland) to be < 3%. After being charge neutralized using a ^{85}Kr neutralizer, a monodisperse aerosol fraction at 100 nm was sampled from the original polydisperse sample with the first differential mobility analyser

121 (DMA) (DMA1). The particles were then passed into a humidification tandem differential mobility

122 analyser (H-TDMA), which is described in detail elsewhere [17,35,36,41], and the diametric hygroscopic

123 growth factors (GF) were measured for both hydration and dehydration humidity cycles. For

124 hydration measurements (deliquescence), the monodisperse aerosol fraction was passed directly from

125 the DMA1 outlet into the RH conditioning flow in the second DMA (DMA2). For dehydration

126 measurements (efflorescence), the monodisperse aerosol fraction was pre-humidified (RH > 90%)

127 using a gas exchange cell (FC100-6, Perma Pure LLC, Lakewood, NJ) before entering the RH

128 conditioning flow in DMA2. The sheath flow rate in DMA1 was 4.5 Lmin⁻¹ and the sheath flow rate

129 in DMA2 was 3.5 Lmin⁻¹ using mass flow controllers (MCP, Alicat Scientific, Inc., Tucson, AZ), and

130 particle counts were measured after DMA2 using a TSI 3776 CPC (TSI, Shoreview, MN). The data

131 were then inverted using the TDMAinv algorithm to calculate the diametric hygroscopic growth

132 factor as the ratio of the diameter of the particles at some RH to the diameter of the particles at RH <

133 10% ($GF = \frac{D_{RH}}{D_{dry}}$) [42]. This process was repeated for each solution w_O listed in Table 1.

134

2.3. Atomic force microscopy

136 Aerosol samples were collected for AFM analysis on Si wafers (Ted Pella, Inc.), which were first

137 cleaned with ethanol and dried using nitrogen gas. Particles were collected onto the Si wafers via

138 electrostatic precipitation using a TSI Nanometer Aerosol Sampler 3089 (TSI, Shoreview, MN)

139 operating at -9 kV with a flow rate of 1 Lmin⁻¹, and analysed immediately. Prior to deposition, the

140 particles were dried to RH < 5% using the same silica desiccator described previously (residence time

141 ~27 s) at ~24 °C. Topographical images and force spectroscopy measurements were collected using a

142 Bruker Dimension Icon PT AFM (Bruker Co., Billerica, MA). The AFM was housed in a vibration

143 isolation chamber, in which the RH and temperature were measured to be 35±2% and 26±1 °C,

144 respectively, over the duration of the measurements. Silicon nitride probes with nominal spring

145 constant of 0.4 Nm⁻¹ were used (Bruker Co., ScanAsyst Air). The spring constant was calibrated

146 before each measurement using the thermal noise method. Topographic images were collected in

147 PeakForce Tapping mode, and force-response measurements were collected using the force ramp

148 function in PeakForce QNM mode with a force threshold of 5 nN and 10 nN. As the tip was indented

149 into the particles, the tip-particle separation distance and force recorded and used to infer viscoelastic

150 properties of the particles (N = 111 particles) [43,44]. The phase of the particles could then be determined

151 as compared to phases of reference materials (NaCl, sucrose). All solutions were prepared at a solute

152 concentration of 5 g/L.

153

## 2.4. Transmission electron microscopy and energy-dispersive X-ray spectroscopy

Aerosol samples were collected for transmission electron microscopy (TEM) analysis on continuous carbon-coated copper grids (200 mesh, Ted Pella, Inc.). Particles were collected onto the grids via electrostatic precipitation using a TSI Nanometer Aerosol Sampler 3089 (TSI, Shoreview, MN) operating at -9 kV with a flow rate of 1 Lmin^{-1}, and analysed immediately. Prior to deposition, the particles were dried to RH < 5% using the same silica desiccator described previously (residence time ~27 s) at ~24 °C. Electron micrographs were collected using a JEOL 1400 TEM or JEOL 2100 TEM with an accelerating voltage of 100 kV or 200 kV, respectively. Elemental analysis of particles was performed using energy-dispersive X-ray spectroscopy (EDS) using an Oxford Instruments X-Max EDS detector (Oxford Instruments, Oxford, UK), which detects characteristic X-rays emitted from electron excitation during TEM measurement. All solutions were prepared at a solute concentration of 5 g/L.

3. Results and discussion

3.1 Hygroscopicity

The diametric hygroscopic growth factor (GF) of each mixture described in Table 1 are shown in Figure 1 as a function of relative humidity (RH). A measured sample of pure porcine gastric mucin (PGM) hygroscopic growth shows continuous water transfer with no evidence of discontinuous phase transitions. Additionally, a polynomial was also fit to the pure PGM data (Figure 1i) and is further discussed in the supplementary material (section S2) to predict diametric hygroscopic growth factor as a function of RH.
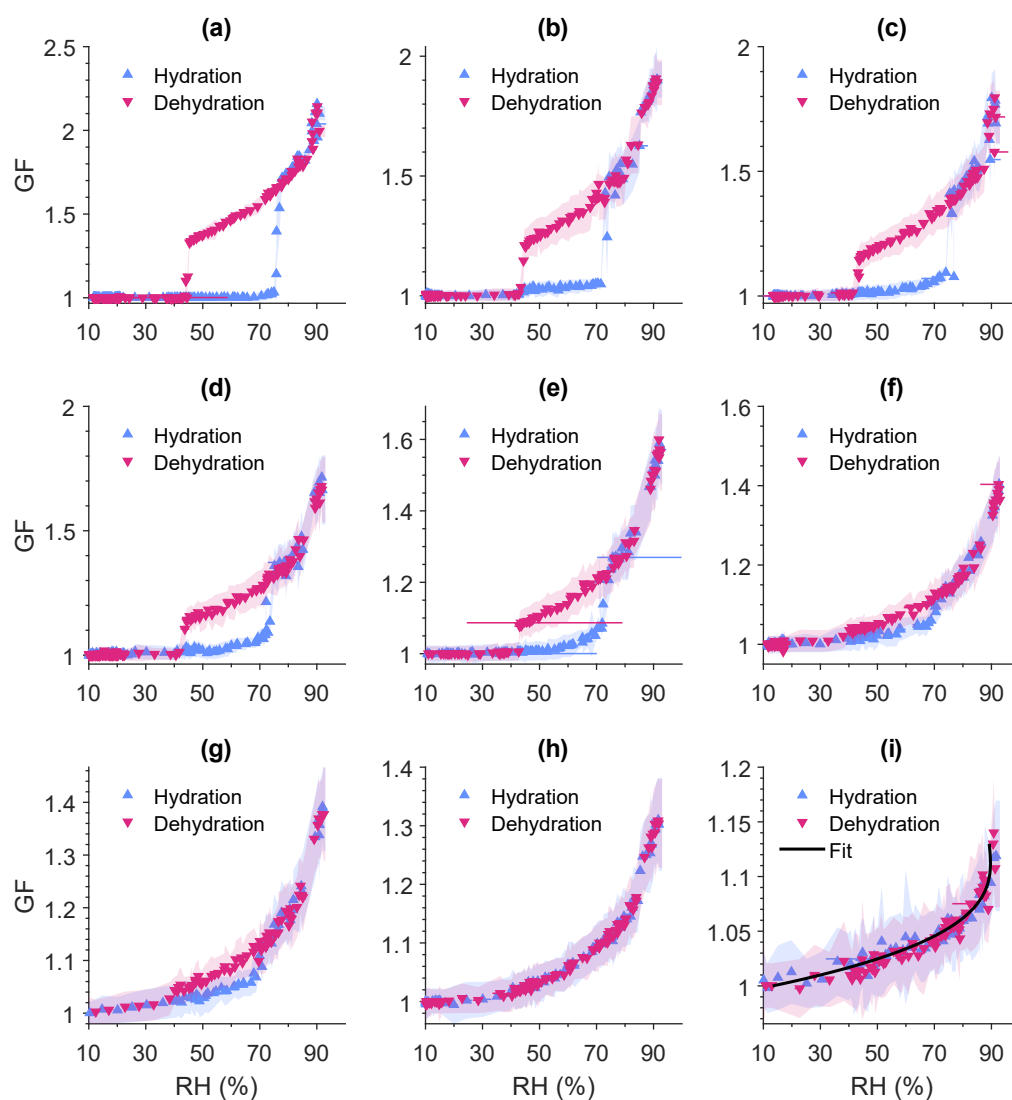
Figure 1. Hygroscopic growth factor (GF) of simulated respiratory fluid particles as a function of relative humidity (RH) for (a) 38%, (b) 70%, (c) 80%, (d) 85%, (e) 90%, (f) 95%, (g) 95.4%, (h) 97%, and (i) 100% porcine gastric mucin by dry solute volume. Discontinuities in the growth indicate liquid ⇌ solid phase transitions. Shaded bands represent the standard error.

As the mass of PGM in each sample increases, the GF at 90% RH (GF_{90}) for each sample decreases, and that the midpoint-RH of efflorescence (ERH_{50}) decreases. A third-order polynomial (equation (S9)) was fit to the experimental GF_{90} data (coefficients in Table S3) as a function of organic volume fraction of dry solute (ϕ_O).

The efflorescence of particles of varying protein concentrations were determined using the dehydration hygroscopic growth measurements. The process to determine ERH_{50} is explained in greater detail in the supplementary material (section S3), but in short, four piecewise linear equations

187   were fit to each dehydration dataset between 30%<RH<60%. In all solution systems, this was

188   sufficient to clearly identify the onset and offset of efflorescence, if it existed. The ERH_{50} was then

189   calculated as the midpoint between the onset and offset of efflorescence and is visualised as a function

190   of organic volume fraction of dry solutes (ϕ_O) in Figure 2.
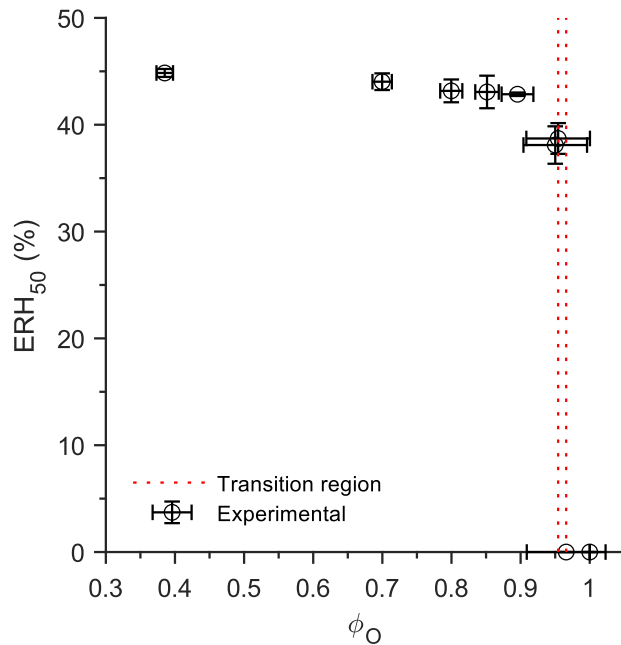

191

192   *Figure 2. Midpoint-efflorescence relative humidity (ERH_{50}) of simulated respiratory fluid aerosols as a function of organic*

193   *volume fraction of dry solutes (ϕ_O). The transition between efflorescing and non-efflorescing particles was observed*

194   *between $0.955<\phi_O<0.97$.*

195   In this case, the ERH gradually decreases with increasing ϕ_O until it can no longer be distinctly

196   observed between $0.955<\phi_O<0.97$. A similar set of measurements using a solution composed of

197   bovine serum albumin (BSA) and NaCl was performed by Mikhailov et al. and identified a similar

198   trend, with efflorescence being suppressed at high ϕ_O [45].

199   The GF_{90} values were calculated from experimental data by fitting a linear model to the GF values

200   between 89.5% and 90.5% RH then and using the function input of 90% RH to calculate the output

201   GF_{90}. Additionally, a physical model (separate solute volume-additivity, SS-VA[45]) and a simplified

202   mixing rule (Zdanovskii-Stokes-Robinson, ZSR[46]) were computed at 90% RH for comparison (Figure

203   3a).

204
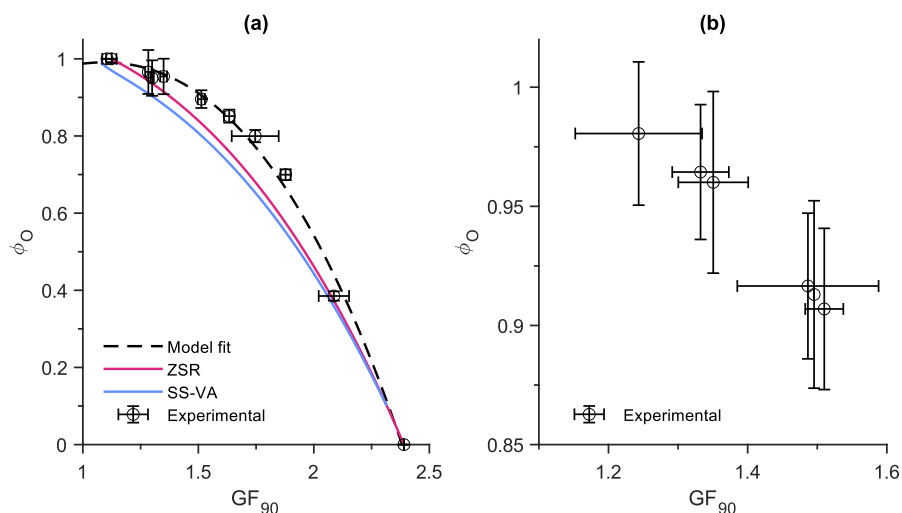
Figure 3. Organic volume fraction of dry solutes (ϕ_O) as a function of particle growth factor at 90% RH (GF$_{90}$) for (a) simulated respiratory fluid solutions of known composition and (b) fitted to prior measured values of human respiratory aerosol as reported in Groth et al. [17]. A physical model (separate solute volume-additivity, SS-VA) and a simple mixing rule (Zdanovskii-Stokes-Robinson, ZSR) are shown as comparison to measured values.

The method to predict ϕ_O from GF$_{90}$ can be extended to previous measurements of human respiratory aerosol hygroscopicity [17]. The GF$_{90}$ of human participants and bovine bronchoalveolar lavage fluid (B-BALF) discussed in Groth et al. were then used to estimate ϕ_O using equation (S9) (Figure 3b, Table S4). Using the GF$_{90}$ to predict ϕ_O estimates that the organic volume fraction of the measured human respiratory aerosol is no less than 91%. As discussed in the supplementary material (section S1), the physical models appear to underpredict the hygroscopicity of PGM, and thus, underpredict the organic volume fraction of the ternary particles. In our prior study, one participant and the B-BALF exhibited the most distinct deliquescence and efflorescence. In comparison to those results, here we measured the hygroscopic behavior of a solution which was composed of 90% PGM by volume, which also exhibited the state hysteresis behavior. Additionally, the next highest predicted organic volume fraction measured in the human samples was 96.01% and does not exhibit efflorescence, consistent with the results of this study (Table S4). This indicates that the threshold for distinct efflorescence may be approximately 96% dry solute organic volume fraction.

3.2 Predicted phase state of simulated respiratory aerosol

The glass transition temperature (T$_g$) of bulk PGM was measured using sorption calorimetry and differential scanning calorimetry (DSC) by Znamenskaya et al., and was reported as a function of weight % of PGM compared to water from 0% to 100% (comparable to weight % observed in PGM aerosol), and is discussed in greater detail in the supplementary material (section S4) [38]. The work of Davies and Viney also investigated the glass transition temperature of PGM, however, the concentration range of PGM investigated in their study (~5-50 %w/w) does not represent the

231   concentration range investigated in our study [47]. Using the hygroscopic growth of PGM measured

232   here (Figure 1), the weight % of PGM in the aerosol can be calculated, and the T_g of PGM aerosol can

233   be reported in terms of RH (Figure 4a). For particles containing PGM and NaCl, prior to

234   efflorescence, the weight % of PGM is calculated relative to the total solution mass. After

235   efflorescence, it is calculated relative only to the water and the PGM. This is a more useful

236   interpretation to predict the phase state of airborne particles in ambient conditions. Figure 4 shows

237   predicted T_g of PGM particles as a function of RH, and includes the assumed particle phase state in

238   each case. For pure PGM aerosol, Figure 4a shows a region of viscoelastic/gelated particles at $T > T_g$

239   (deformable, soft) and vitreous particles at $T < T_g$ (rigid, hard). Figure 4b shows the case where the

240   particles also contain NaCl but do not effloresce ($\phi_O = 0.97$) and shows comparative behavior to

241   Figure 4a. For the case where NaCl is present in the system and at high enough concentrations to

242   exhibit efflorescence ($\phi_O < 0.96$), the proteins within the particles are expected to exhibit the same

243   behavior as in Figure 4a and b, and the NaCl will be crystalline at RH < ERH and aqueous otherwise

244   (Figure 4c,d). Different configurations of these phases are possible depending on the ambient

245   conditions and will likely lead to different particle morphologies. These four-phase systems are shown

246   most clearly in Figure 4c. It is important to note, that these diagrams do not denote hard phase

247   transition boundaries and require a sufficient temperature and RH differential. Given that these phases

248   were not measured explicitly in ternary SRF particles, there may be more complex physicochemical

249   behavior affecting potential glass transition which cannot be predicted from calorimetry.

250

251
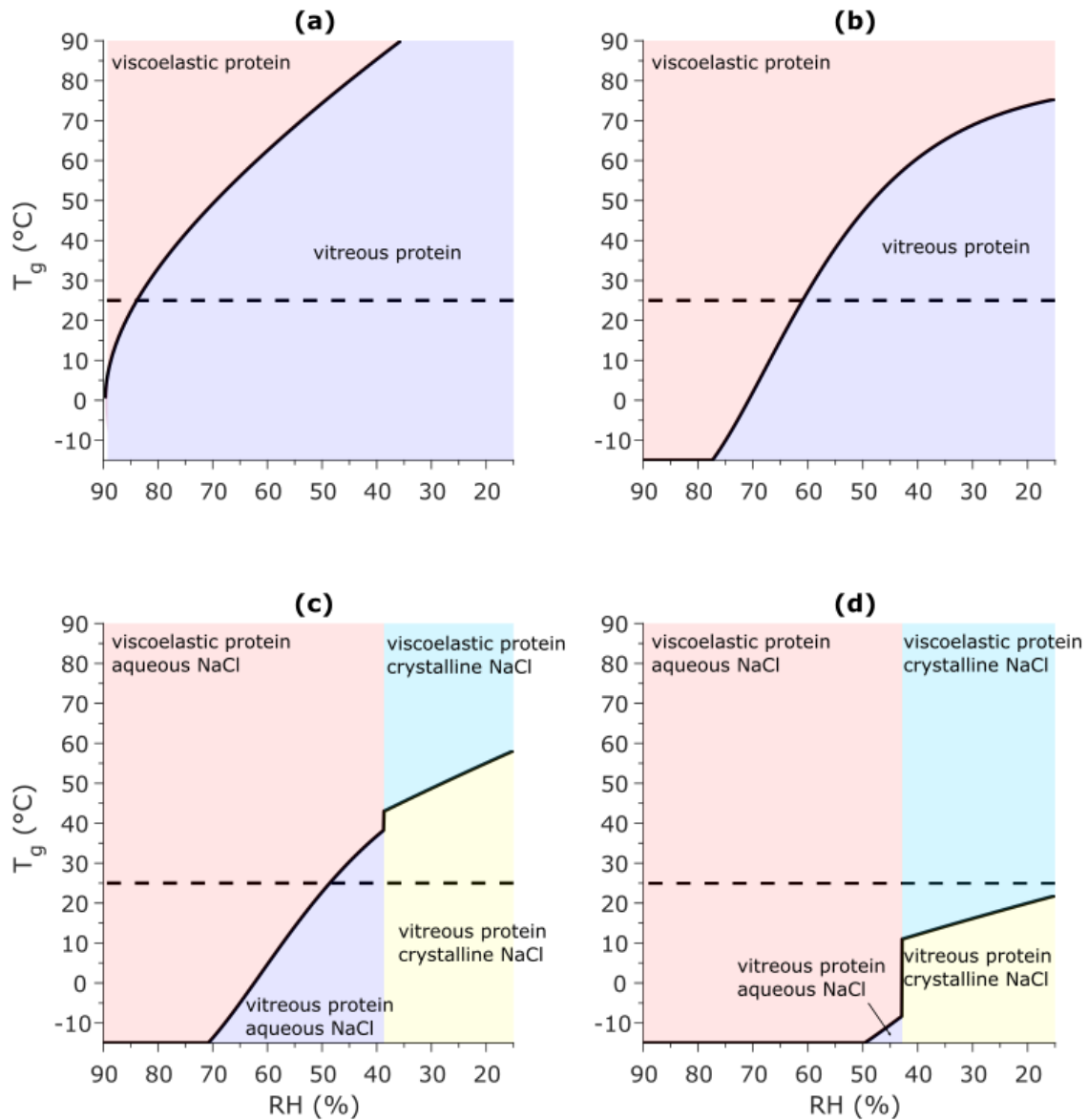
Figure 4. Predicted glass transition temperature (T_g) of 100 nm simulated respiratory fluid particles as a function of RH for

(a) 100%, (b) 97%, (c) 95% and (d) 90% porcine gastric mucin (PGM) by dry solute volume. The shaded regions represent

distinct particle phases and morphologies, and the dashed line is a visual reference for 25 °C.

255   In the case of the samples measured in this study, it is expected that the dynamic phase behavior of

256   the particles would be consistent with the results reported by Huynh et al. [29]. Immediately at

257   generation, the particles will be liquid droplets and through dehydration, the particles would transition

258   from a liquid to an amorphous solid through aggregation and gelation of proteins (Figure 4, red

259   region) [29]. As these particles further release water (decreasing RH), the viscosity of the viscoelastic

260 protein will increase and eventually vitrify with sufficiently high drying rates (Figure 4, dark-blue

261 region). This process was incorporated by Dette et al. as the 'MARBLES' technique to observe glass

262 transition in organic aerosols [48]. For lower organic fractions, and thus higher inorganic fractions, it

263 becomes less probable that the particles will vitrify in room conditions due to the decreasing glass

264 transition temperature (Figure 4d).

265

3.3 Measured morphology and phase state of dry particles

267 To confirm the morphology and phases predicted earlier (Figure 4), simulated respiratory fluid (SRF)

268 particles were investigated using transmission electron microscopy (TEM) and atomic force

269 microscopy (AFM). The observed morphologies could be primarily classified by the behavior of the

270 NaCl as monocrystalline (**Error! Reference source not found.**b,c,d), polycrystalline (Figure 5c,d),

271 microcrystalline (Figure 7), or non-crystalline (Figure 8). The differing observed morphologies

272 suggest that the distribution of PGM within the aerosols was not homogeneous. It is assumed that the

273 distribution of aqueous NaCl is uniform due to high water solubility and thus complete dissociation

274 within the solution. Therefore, the organic volume fraction of the droplets will be a distribution of

275 what was measured in the bulk, indicating that the composition of each individual droplet will affect

276 the morphology of the dried particles [36,49].
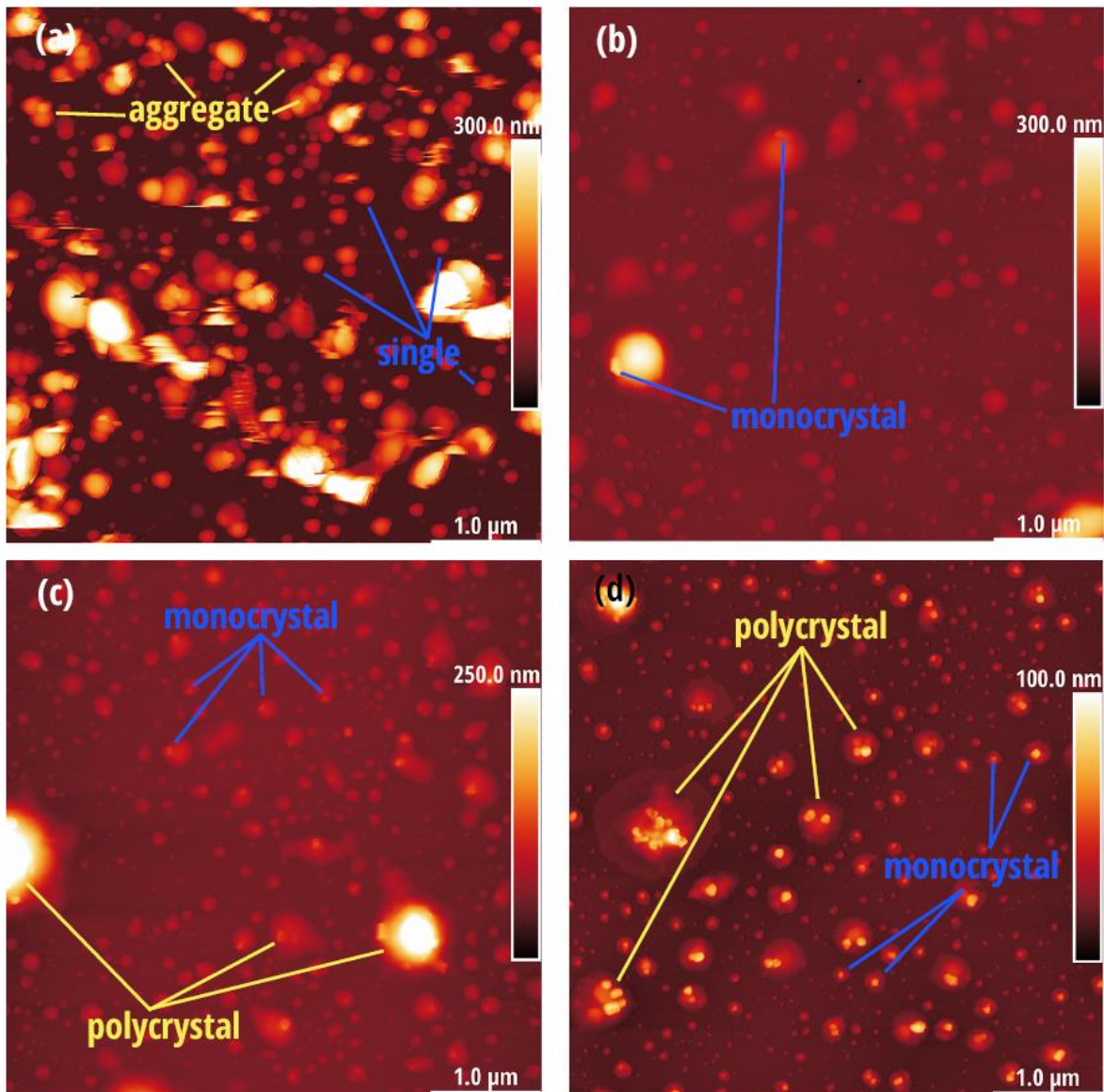
Figure 5. Representative atomic force micrographs of simulated respiratory fluid particles with (a) 100%, (b) 97%, (c) 95%, and (d) 90% mucin by dry solute volume, deposited on a Si wafer. Images are annotated to demonstrate different particle morphologies.

Physiologically relevant SRF particles were collected onto Si wafers for AFM with 90%, 95%, 97%, and 100% PGM by dry solute volume. The pure PGM aerosol AFM micrograph (Figure 5a) shows that the deposited protein aerosol could be either a single protein or an aggregate (annotated on image). In AFM micrographs of NaCl/PGM aerosol, the same frequency of protein aggregates is not observed. Particles with crystalline NaCl were observed in all cases, with varying frequency. For 97% PGM particles, ~31% of particles (out of N = 107 particles total) had a single crystal morphology. For 90% PGM particles, using TEM micrographs, ~59% of crystalline particles (out of N = 193 particles total) had a single crystal morphology (median area equivalent diameter = 48 nm). Polycrystalline NaCl was observed in ~41% of crystalline particles in 90% PGM particles (median area equivalent diameter = 145 nm). Higher drying rates may influence the nucleation of polycrystal structures, where

291 upon drying, the viscosity of the organic phase increases and will kinetically limit the diffusion of

292 water out of the particles [50–54]. At generation, where RH ≈100%, the particles are likely homogeneous

293 liquid droplets. Upon dehydration, liquid-liquid phase separation (LLPS) between organic and

294 inorganic phases [55,56] or aggregation of the proteins will occur. The aqueous inorganics form multiple

295 inclusions, and will then not coalesce into a single inclusion before nucleation due to the inhibitive

296 viscosity of the organic matrix, resulting in multiple crystal structures [57,58]. Works have shown that

297 LLPS for organic/organic mixed aerosol [55], and for organic/inorganic mixed aerosol [56], can occur for

298 organics with O:C < 0.44 and O:C < 0.7, respectively. The O:C ratio of mucin 5AC is ~0.35

299 (UniProtKB:P98088), which suggests it may be a candidate for LLPS. In the case of PGM, which is

300 relatively insoluble in water compared to NaCl, it is expected that any LLPS will occur at high RH

301 prior to the loss of sufficient water for the PGM to remain in solution. It is also important to note that

302 the location of the single NaCl crystals within these particles is consistently on the side of the particle,

303 whereas polycrystalline NaCl crystals are distributed throughout the particles. We could not determine

304 conclusively if these crystals were embedded within the protein or located at the particle-atmosphere

305 interface.

306
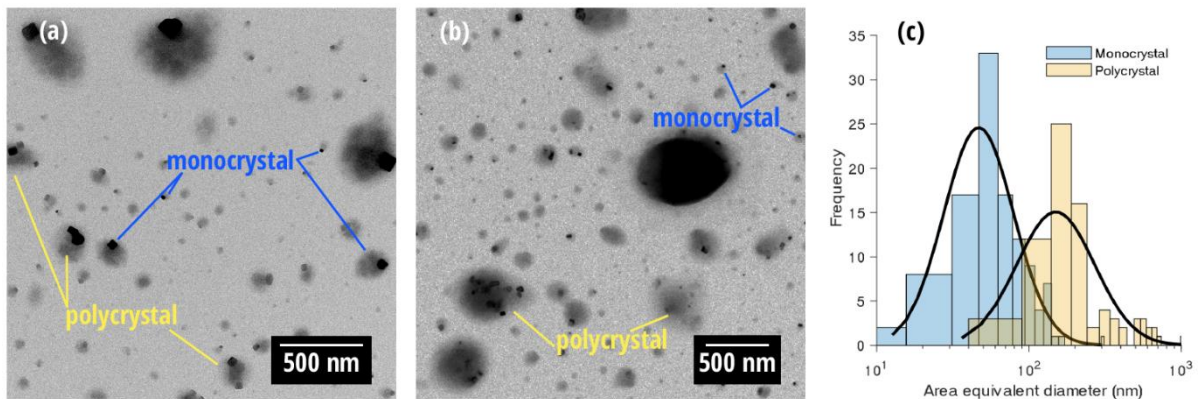
307 *Figure 6. Transmission electron micrographs of simulated respiratory fluid particles with (a) 95% and (b) 90% mucin by dry*
308 *solute volume, along with (c) the size distribution of particle morphologies for 90% mucin by dry solute volume for N = 193*
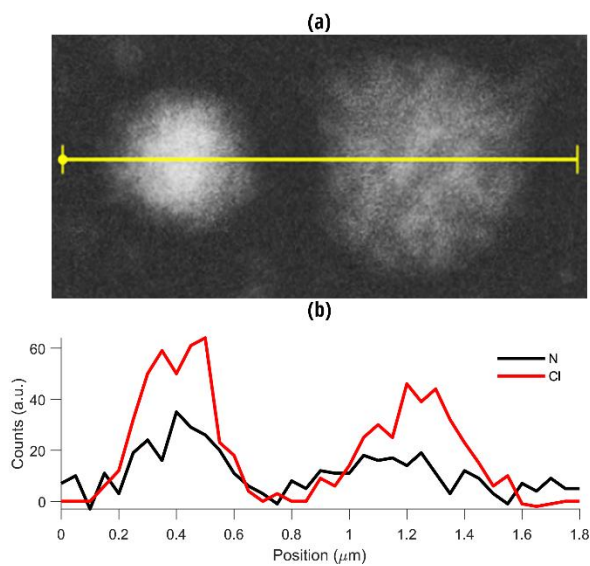309 *particles.*

310
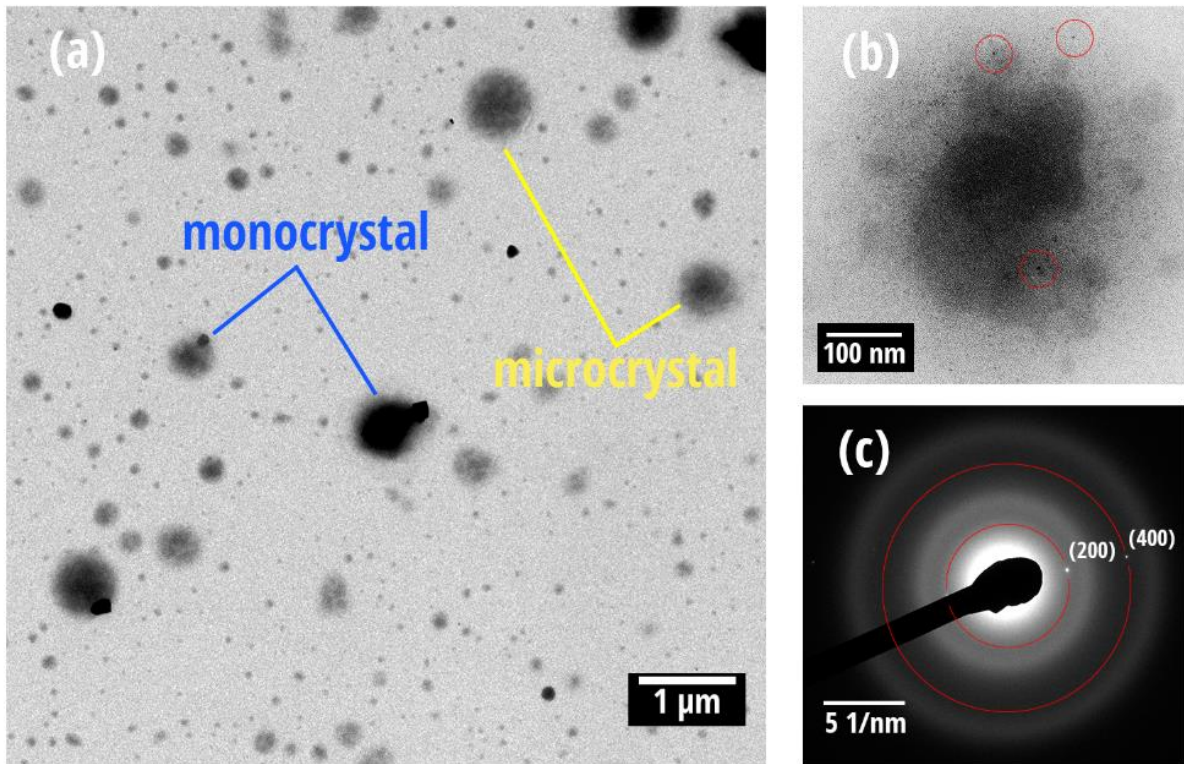
311

316 In 97% PGM particles, both amorphous and particles with NaCl microcrystals were observed.

317 Microcrystalline NaCl was observed in some particles (Figure 7a,b), with select area electron

318 diffraction (SAED) analysis showing d-spacing corresponding to the (200) and (400) lattice planes of

319 NaCl (Figure 7c). Amorphous particles were observed using energy-dispersive X-ray spectroscopy

320 (EDS). An EDS linescan measurement was taken (Figure 8) on SRF particles which shows that

321 chlorine counts increased with particle height. Nitrogen counts are also shown as a reference for

322 PGM, as the other major elements in PGM (C, O) are also present in the polymer coating of the TEM

323 grid or are too light to be detected via EDS (H). The size of the high contrast NaCl spots in Figure 7b

324 are ~3 nm and are distributed relatively sparsely throughout the particle. Because Cl counts increase

325 with particle height, it indicates that the Cl is distributed homogeneously throughout the particles,

326 rather than NaCl microcrystals. For 97% PGM particles, ~69% of particles had no clear crystal

327 structure (out of N = 107 particles total). These morphologies are either amorphous protein with

328 Na/Cl distributed homogeneously throughout the particle or are amorphous protein with NaCl

329 microcrystals distributed throughout the particle (the exact frequency could not be determined). In the

330 cases of higher NaCl concentration SRF systems, some particles were also observed which did not

331 contain distinct crystals. The reason for this is not understood but may be due to variation in

332 composition across different particles. Significant organic enrichment may limit efflorescence within

333 particles due to increasing viscosity during drying, which prevents sufficient quantities of NaCl from

334 coalescing and crystallizing. The crystallization was not observed in H-TDMA measurements,

335 indicating that perhaps for the 97% PGM SRF additionally equilibration time was required for

336 efflorescence, or that the morphology of particles deposited on a surface can differ from those

337 suspended in the air.

338
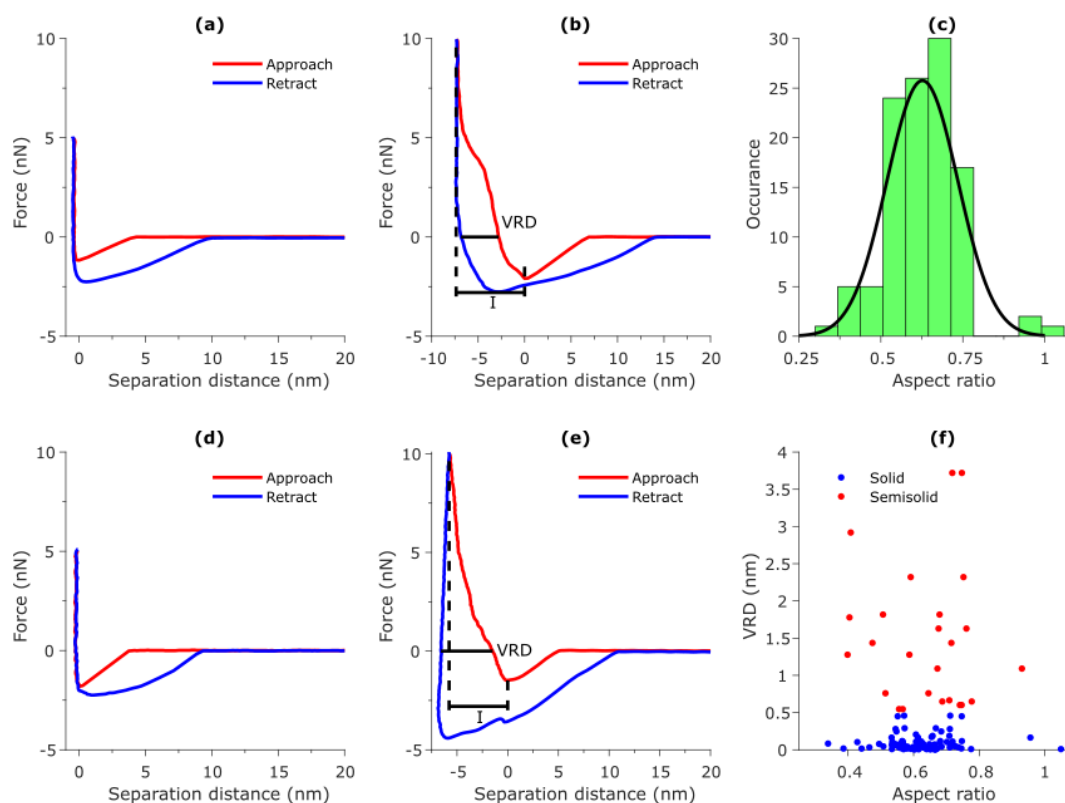
339

340

Figure 8. Energy-dispersive X-ray spectroscopy (EDS) linescan of amorphous simulated respiratory fluid (SRF) particles, with 97% protein by dry solute volume. (a) shows the reference scanning transmission electron micrograph (STEM) and (b) shows the X-ray count profile for nitrogen and chlorine.

344

345

Figure 9. Example representative force response curves for pure porcine gastric mucin (PGM) particles of height (a) 107

nm and (b) 132 nm. The particles were deposited on a Si wafer and a maximum applied force of 5 or 10 nN at 35% RH. The

determination of indentation depth (I) and viscoelastic response distance (VRD) are shown graphically (b, e). Figures (a)

and (b) show representative force response of solid and semisolid PGM particles, respectively. Shown also are force

response curves for (d) NaCl (solid) and © sucrose (semisolid) particle for reference. Figure (c) shows the aspect ratio (AR)

distribution for N = 111 PGM particles. Figure (f) shows the VRD of the PGM particles as a function of AR.

The viscoelastic response distance (VRD) and relative indentation depth (RID) of pure PGM particles

~100 nm and larger (N=111) were measured through AFM force spectroscopy. In each force response

measurement, the tip is indented into the particle until the force threshold (5 nN or 10 nN) is reached.

The RID is calculated as the ratio of the indentation depth and the height of the particle. For solid

particles, the RID is expected to be low because the tip cannot indent a large distance into the

particles, and for liquid particles the RID should be approximately 1. The VRD is measured through

hysteresis in the force response measurements (at force = 0) due to viscoelastic properties of the

material. The results presented by Lee et al. and Ray et al. suggest that particles with VRD < 0.5 nm

are solid and with VRD > 0.5 nm are viscoelastic semisolids [43,44]. From the 111 particles measured

using force spectroscopy in this study, ~77% were determined to be solid, and ~23% were determined

to be viscoelastic semisolid. The average aspect ratio (AR) of the particles measured here was

0.63±0.01 (Figure 9c) and was not significantly affected by particle phase (Table S7). Representative

force response curves were collected for representative solid (NaCl, Figure 9d) and semisolid

365 (sucrose, Figure 9e) particles. The NaCl and sucrose force response curves shown here (Figure 9d,e)

366 agree with previously reported results [43,44].

367

4. Implications of vitreous protein aerosol

369 The systems investigated here show comparative behavior to that of human respiratory aerosol. In the

370 context of airborne virus transmission, the predicted phase sate of the particles in typical ambient

371 room conditions is most important. The dynamic transport of respiratory aerosol begins in the

372 respiratory tract of one individual at approximately 37 °C and 100% relative humidity (RH). The final

373 phase of transport will involve reinhalation of a particle to another individual, also at 37 °C and 100%

374 RH. Between these phases, the second phase of transport is spatiotemporally dependent, and will vary

375 between climatic and indoor conditions. From the morphology and phases discussed earlier, it is

376 evident that typical indoor air conditions (30%<RH<60%, 20 °C<T<25 °C) may be a problematic

377 intersection of respiratory aerosol physicochemistry due to numerous possible state configurations,

378 which may affect virus viability. During the process of respiratory aerosol transport, it is evident that

379 the particles will experience a large temperature and RH differential (~10 °C and ~50% RH over ~1

380 second during expiration into room air). Rapid cooling and/or drying rates are typically required for

381 glass transitions, which further suggests that glass transition of respiratory aerosols are possible [48,59].

382 As discussed earlier, these respiratory particles can be classified as either efflorescing (ϕ_O<0.96,

383 Figure 4c,d) or non-efflorescing (ϕ_O>0.96, Figure 4a,b). Efflorescing particles below the

384 efflorescence RH (ERH) will limit the exposure to concentrated aqueous salts and promote the

385 viability of viruses such as influenza A virus H3N2 and human rhinovirus-16 [8,9], while having lower

386 viability in moderate RH (60%<RH>ERH) (Figure S4). High temperature environments will favor

387 viscoelastic protein (Figure 4, red and light-blue regions), whereas low temperature environments will

388 favor vitreous protein (Figure 4, dark-blue and yellow regions). At RH>ERH, the NaCl will be in an

389 aqueous phase (Figure 4, red and dark-blue regions), and low RH environments will favor crystalline

390 NaCl (Figure 4, light-blue and yellow regions). If the particles are below the threshold for glass

391 transition, the organic phase will be viscous and limit kinetic processes within the particle and is

392 assumed that they will be kinetically 'frozen' at the RH at the transition boundary. Given sufficient

393 time, the particles will relax to their stable equilibrium with the ambient environment. Viruses in non-

394 effloressing particles (high ϕ_O) will likely have higher viability in all RH situations due to lower ion

395 concentration (limited disinfectant effect) and a protein-enriched microenvironment. Additionally, the

396 high viscosity of low-RH non-effloressing particles will further promote virus viability by limiting the

397 molecular transport of oxidizing species and other harmful reactants [29]. Therefore, the composition of

398 the respiratory particles must be directly linked with the phase state and morphology and depend on

399 the ambient conditions, especially RH and T.

400 Although lacking the complexity of real respiratory fluid, the results of this study expand on prior

401 physicochemical characterisation of simulated respiratory fluid [8,29,33,34]. Future investigations

402 involving increasingly representative compositions may be useful (e.g., the inclusion of surfactants

403 and different inorganics, or animal respiratory fluid), although it is unlikely that completely

404 simulating the complexity of both the composition and production mechanisms of respiratory aerosol

405 is possible. Additional *in situ* experiments to confirm morphology and phase in levitated droplets are

406 also desired. For further airborne virology research, it is important to consider the composition of the

407 solution more carefully, using higher protein concentration than used in prior studies.

408

Authors' Contributions

410 All authors contributed to experimental design. R.G., S.N., and G.R.J. contributed to experimentation.
411 R.G. and Z.R. contributed to data analysis and interpretation. All authors contributed to the
412 manuscript drafting and revision.

Competing Interests

414 The authors declare no competing interests.

Supporting Information

418 Supporting manuscript (8 pages) which contains 4 figures and 7 tables.

424

References

426 (1) Asadi, S.; Wexler, A. S.; Cappa, C. D.; Barreda, S.; Bouvier, N. M.; Ristenpart, W. D. Aerosol
427   Emission and Superemission during Human Speech Increase with Voice Loudness. *Scientific*
428   *Reports* **2019**, *9* (1), 2348. https://doi.org/10.1038/s41598-019-38808-z.
429 (2) Lindsley, W. G.; Blachere, F. M.; Beezhold, D. H.; Thewlis, R. E.; Noorbakhsh, B.; Othumpangat,
430   S.; Goldsmith, W. T.; McMillen, C. M.; Andrew, M. E.; Burrell, C. N.; Noti, J. D. Viable Influenza
431   A Virus in Airborne Particles Expelled during Coughs versus Exhalations. *Influenza Other Respi*
432   *Viruses* **2016**, *10* (5), 404–413. https://doi.org/10.1111/irv.12390.
433 (3) Morawska, L.; Milton, D. K. It Is Time to Address Airborne Transmission of Coronavirus
434   Disease 2019 (COVID-19). *Clinical Infectious Diseases* **2020**, ciaa939.
435   https://doi.org/10.1093/cid/ciaa939.

436   (4)   Morawska, L.; Cao, J. Airborne Transmission of SARS-CoV-2: The World Should Face the
437   Reality. *Environment International* **2020**, *139*, 105730.
438   https://doi.org/10.1016/j.envint.2020.105730.
439   (5)   Greenhalgh, T.; Jimenez, J. L.; Prather, K. A.; Tufekci, Z.; Fisman, D.; Schooley, R. Ten Scientific
440   Reasons in Support of Airborne Transmission of SARS-CoV-2. *The Lancet* **2021**, *397* (10285),
441   1603–1605. https://doi.org/10.1016/S0140-6736(21)00869-2.
442   (6)   Yang, W.; Marr, L. C. Dynamics of Airborne Influenza A Viruses Indoors and Dependence on
443   Humidity. *PLoS ONE* **2011**, *6* (6), e21481. https://doi.org/10.1371/journal.pone.0021481.
444   (7)   Yang, W.; Elankumaran, S.; Marr, L. C. Relationship between Humidity and Influenza A
445   Viability in Droplets and Implications for Influenza's Seasonality. *PLoS ONE* **2012**, *7* (10),
446   e46789. https://doi.org/10.1371/journal.pone.0046789.
447   (8)   Niazi, S.; Groth, R.; Cravigan, L.; He, C.; Tang, J. W.; Spann, K.; Johnson, G. R. Susceptibility of
448   an Airborne Common Cold Virus to Relative Humidity. *Environ. Sci. Technol.* **2021**, *55* (1), 499–
449   508. https://doi.org/10.1021/acs.est.0c06197.
450   (9)   Niazi, S.; Short, K. R.; Groth, R.; Cravigan, L.; Spann, K.; Ristovski, Z.; Johnson, G. R. Humidity-
451   Dependent Survival of an Airborne Influenza A Virus: Practical Implications for Controlling
452   Airborne Viruses. *Environ. Sci. Technol. Lett.* **2021**, *8* (5), 412–418.
453   https://doi.org/10.1021/acs.estlett.1c00253.
454   (10)   Shaman, J.; Kohn, M. Absolute Humidity Modulates Influenza Survival, Transmission, and
455   Seasonality. *Proceedings of the National Academy of Sciences* **2009**, *106* (9), 3243–3248.
456   https://doi.org/10.1073/pnas.0806852106.
457   (11)   Tamerius, J. D.; Shaman, J.; Alonso, W. J.; Bloom-Feshbach, K.; Uejio, C. K.; Comrie, A.; Viboud,
458   C. Environmental Predictors of Seasonal Influenza Epidemics across Temperate and Tropical
459   Climates. *PLoS Pathogens* **2013**, *9* (3), e1003194.
460   https://doi.org/10.1371/journal.ppat.1003194.
461   (12)   Tang, J. W. The Effect of Environmental Parameters on the Survival of Airborne Infectious
462   Agents. *Journal of The Royal Society Interface* **2009**, *6* (suppl_6).
463   https://doi.org/10.1098/rsif.2009.0227.focus.
464   (13)   Niazi, S.; Groth, R.; Spann, K.; Johnson, G. R. The Role of Respiratory Droplet Physicochemistry
465   in Limiting and Promoting the Airborne Transmission of Human Coronaviruses: A Critical
466   Review. *Environmental Pollution* **2020**, 115767.
467   https://doi.org/10.1016/j.envpol.2020.115767.
468   (14)   Johnson, G. R.; Morawska, L. The Mechanism of Breath Aerosol Formation. *Journal of Aerosol*
469   *Medicine and Pulmonary Drug Delivery* **2009**, *22* (3), 229–237.
470   https://doi.org/10.1089/jamp.2008.0720.
471   (15)   Johnson, G. R.; Morawska, L.; Ristovski, Z. D.; Hargreaves, M.; Mengersen, K.; Chao, C. Y. H.;
472   Wan, M. P.; Li, Y.; Xie, X.; Katoshevski, D.; Corbett, S. Modality of Human Expired Aerosol Size
473   Distributions. *Journal of Aerosol Science* **2011**, *42* (12), 839–851.
474   https://doi.org/10.1016/j.jaerosci.2011.07.009.
475   (16)   Morawska, L.; Johnson, G. R.; Ristovski, Z. D.; Hargreaves, M.; Mengersen, K.; Corbett, S.;
476   Chao, C. Y. H.; Li, Y.; Katoshevski, D. Size Distribution and Sites of Origin of Droplets Expelled
477   from the Human Respiratory Tract during Expiratory Activities. *Journal of Aerosol Science*
478   **2009**, *40* (3), 256–269. https://doi.org/10.1016/j.jaerosci.2008.11.002.
479   (17)   Groth, R.; Cravigan, L. T.; Niazi, S.; Ristovski, Z.; Johnson, G. R. In Situ Measurements of
480   Human Cough Aerosol Hygroscopicity. *Journal of The Royal Society Interface* **2021**, *18* (178),
481   9.
482   (18)   Walker, J. S.; Archer, J.; Gregson, F. K. A.; Michel, S. E. S.; Bzdek, B. R.; Reid, J. P. Accurate
483   Representations of the Microphysical Processes Occurring during the Transport of Exhaled
484   Aerosols and Droplets. *ACS Cent. Sci.* **2021**, *7* (1), 200–209.
485   https://doi.org/10.1021/acscentsci.0c01522.

486   (19)   Fahy, J. V.; Dickey, B. F. Airway Mucus Function and Dysfunction. *The New England Journal of*
487   *Medicine* **2010**, *363* (23), 2233–2247. https://doi.org/10.1056/NEJMra0910061.
488   (20)   Thornton, D. J.; Rousseau, K.; McGuckin, M. A. Structure and Function of the Polymeric
489   Mucins in Airways Mucus. *Annu. Rev. Physiol.* **2008**, *70* (1), 459–486.
490   https://doi.org/10.1146/annurev.physiol.70.113006.100702.
491   (21)   Boisa, N.; Elom, N.; Dean, J. R.; Deary, M. E.; Bird, G.; Entwistle, J. A. Development and
492   Application of an Inhalation Bioaccessibility Method (IBM) for Lead in the PM10 Size Fraction
493   of Soil. *Environment International* **2014**, *70*, 132–142.
494   https://doi.org/10.1016/j.envint.2014.05.021.
495   (22)   Effros, R. M.; Hoagland, K. W.; Bosbous, M.; Castillo, D.; Foss, B.; Dunning, M.; Gare, M.; Lin,
496   W.; Sun, F. Dilution of Respiratory Solutes in Exhaled Condensates. *American Journal of*
497   *Respiratory and Critical Care Medicine* **2002**, *165* (5), 663–669.
498   (23)   Nicas, M.; Nazaroff, W. W.; Hubbard, A. Toward Understanding the Risk of Secondary
499   Airborne Infection: Emission of Respirable Pathogens. *Journal of Occupational and*
500   *Environmental Hygiene* **2005**, *2* (3), 143–154. https://doi.org/10.1080/15459620590918466.
501   (24)   Kormuth, K. A.; Lin, K.; Prussin, A. J.; Vejerano, E. P.; Tiwari, A. J.; Cox, S. S.; Myerburg, M. M.;
502   Lakdawala, S. S.; Marr, L. C. Influenza Virus Infectivity Is Retained in Aerosols and Droplets
503   Independent of Relative Humidity. *The Journal of Infectious Diseases* **2018**, *218* (5), 739–747.
504   https://doi.org/10.1093/infdis/jiy221.
505   (25)   Morris, D. H.; Yinda, K. C.; Gamble, A.; Rossine, F. W.; Huang, Q.; Bushmaker, T.; Fischer, R. J.;
506   Matson, M. J.; Van Doremalen, N.; Vikesland, P. J.; Marr, L. C.; Munster, V. J.; Lloyd-Smith, J.
507   O. Mechanistic Theory Predicts the Effects of Temperature and Humidity on Inactivation of
508   SARS-CoV-2 and Other Enveloped Viruses. *eLife* **2021**, *10*, e65902.
509   https://doi.org/10.7554/eLife.65902.
510   (26)   Prussin, A. J.; Schwake, D. O.; Lin, K.; Gallagher, D. L.; Buttling, L.; Marr, L. C. Survival of the
511   Enveloped Virus Phi6 in Droplets as a Function of Relative Humidity, Absolute Humidity, and
512   Temperature. *Applied and Environmental Microbiology* **2018**, *84* (12), e00551-18,
513   /aem/84/12/e00551-18.atom. https://doi.org/10.1128/AEM.00551-18.
514   (27)   Lin, K.; Schulte, C. R.; Marr, L. C. Survival of MS2 and Φ6 Viruses in Droplets as a Function of
515   Relative Humidity, PH, and Salt, Protein, and Surfactant Concentrations. *PLoS ONE* **2020**, *15*
516   (12), e0243505. https://doi.org/10.1371/journal.pone.0243505.
517   (28)   Pan, M.; Carol, L.; Lednicky, J. A.; Eiguren-Fernandez, A.; Hering, S.; Fan, Z. H.; Wu, C.-Y.
518   Determination of the Distribution of Infectious Viruses in Aerosol Particles Using Water-Based
519   Condensational Growth Technology and a Bacteriophage MS2 Model. *Aerosol Science and*
520   *Technology* **2019**, 1–11. https://doi.org/10.1080/02786826.2019.1581917.
521   (29)   Huynh, E.; Olinger, A.; Woolley, D.; Kohli, R. K.; Choczynski, J. M.; Davies, J. F.; Lin, K.; Marr, L.
522   C.; Davis, R. D. Evidence for a Semisolid Phase State of Aerosols and Droplets Relevant to the
523   Airborne and Surface Survival of Pathogens. *Proc Natl Acad Sci USA* **2022**, *119* (4),
524   e2109750119. https://doi.org/10.1073/pnas.2109750119.
525   (30)   Shiraiwa, M.; Ammann, M.; Koop, T.; Poschl, U. Gas Uptake and Chemical Aging of Semisolid
526   Organic Aerosol Particles. *Proceedings of the National Academy of Sciences* **2011**, *108* (27),
527   11003–11008. https://doi.org/10.1073/pnas.1103045108.
528   (31)   Shiraiwa, M.; Li, Y.; Tsimpidi, A. P.; Karydis, V. A.; Berkemeier, T.; Pandis, S. N.; Lelieveld, J.;
529   Koop, T.; Pöschl, U. Global Distribution of Particle Phase State in Atmospheric Secondary
530   Organic Aerosols. *Nature Communications* **2017**, *8*, 15002.
531   https://doi.org/10.1038/ncomms15002.
532   (32)   Virtanen, A.; Joutsensaari, J.; Koop, T.; Kannosto, J.; Yli-Pirilä, P.; Leskinen, J.; Mäkelä, J. M.;
533   Holopainen, J. K.; Pöschl, U.; Kulmala, M.; Worsnop, D. R.; Laaksonen, A. An Amorphous Solid
534   State of Biogenic Secondary Organic Aerosol Particles. *Nature* **2010**, *467* (7317), 824–827.
535   https://doi.org/10.1038/nature09455.

536   (33)   Vejerano, E. P.; Marr, L. C. Physico-Chemical Characteristics of Evaporating Respiratory Fluid
537   Droplets. *Journal of The Royal Society Interface* **2018**, *15* (139), 20170939.
538   https://doi.org/10.1098/rsif.2017.0939.

539   (34)   Davies, J. F.; Price, C. L.; Choczynski, J.; Kohli, R. K. Hygroscopic Growth of Simulated Lung
540   Fluid Aerosol Particles under Ambient Environmental Conditions. *Chem. Commun.* **2021**,
541   10.1039.D1CC00066G. https://doi.org/10.1039/D1CC00066G.

542   (35)   Johnson, G. R.; Fletcher, C.; Meyer, N.; Modini, R.; Ristovski, Z. D. A Robust, Portable H-TDMA
543   for Field Use. *Journal of Aerosol Science* **2008**, *39* (10), 850–861.
544   https://doi.org/10.1016/j.jaerosci.2008.05.005.

545   (36)   Cravigan, L. T.; Mallet, M. D.; Vaattovaara, P.; Harvey, M. J.; Law, C. S.; Modini, R. L.; Russell, L.
546   M.; Stelcer, E.; Cohen, D. D.; Olsen, G.; Safi, K.; Burrell, T. J.; Ristovski, Z. Sea Spray Aerosol
547   Organic Enrichment, Water Uptake and Surface Tension Effects. *Atmos. Chem. Phys.* **2020**, *20*
548   (13), 7955–7977. https://doi.org/10.5194/acp-20-7955-2020.

549   (37)   Johnson, G. R. Hygroscopic Behavior of Partially Volatilized Coastal Marine Aerosols Using the
550   Volatilization and Humidification Tandem Differential Mobility Analyzer Technique. *J.*
551   *Geophys. Res.* **2005**, *110* (D20), D20203. https://doi.org/10.1029/2004JD005657.

552   (38)   Znamenskaya, Y.; Sotres, J.; Engblom, J.; Arnebrant, T.; Kocherbitov, V. Effect of Hydration on
553   Structural and Thermodynamic Properties of Pig Gastric and Bovine Submaxillary Gland
554   Mucins. *The Journal of Physical Chemistry B* **2012**, *116* (16), 5047–5055.
555   https://doi.org/10.1021/jp212495t.

556   (39)   Rose, M. C.; Voynow, J. A. Respiratory Tract Mucin Genes and Mucin Glycoproteins in Health
557   and Disease. *Physiological Reviews* **2006**, *86* (1), 245–278.
558   https://doi.org/10.1152/physrev.00010.2005.

559   (40)   Wagner, C. E.; Turner, B. S.; Rubinstein, M.; McKinley, G. H.; Ribbeck, K. A Rheological Study
560   of the Association and Dynamics of MUC5AC Gels. *Biomacromolecules* **2017**, *18* (11), 3654–
561   3664. https://doi.org/10.1021/acs.biomac.7b00809.

562   (41)   Duplissy, J.; Gysel, M.; Sjogren, S.; Meyer, N.; Good, N.; Kammermann, L.; Michaud, V.;
563   Weigel, R.; Martins dos Santos, S.; Gruening, C.; Villani, P.; Laj, P.; Sellegri, K.; Metzger, A.;
564   McFiggans, G. B.; Wehrle, G.; Richter, R.; Dommen, J.; Ristovski, Z.; Baltensperger, U.;
565   Weingartner, E. Intercomparison Study of Six HTDMAs: Results and Recommendations.
566   *Atmos. Meas. Tech.* **2009**, *2* (2), 363–378. https://doi.org/10.5194/amt-2-363-2009.

567   (42)   Gysel, M.; McFiggans, G. B.; Coe, H. Inversion of Tandem Differential Mobility Analyser
568   (TDMA) Measurements. *Journal of Aerosol Science* **2009**, *40* (2), 134–151.
569   https://doi.org/10.1016/j.jaerosci.2008.07.013.

570   (43)   Lee, H. D.; Ray, K. K.; Tivanski, A. V. Solid, Semisolid, and Liquid Phase States of Individual
571   Submicrometer Particles Directly Probed Using Atomic Force Microscopy. *Anal. Chem.* **2017**,
572   *89* (23), 12720–12726. https://doi.org/10.1021/acs.analchem.7b02755.

573   (44)   Ray, K. K.; Lee, H. D.; Gutierrez, M. A.; Chang, F. J.; Tivanski, A. V. Correlating 3D Morphology,
574   Phase State, and Viscoelastic Properties of Individual Substrate-Deposited Particles. *Anal.*
575   *Chem.* **2019**, *91* (12), 7621–7630. https://doi.org/10.1021/acs.analchem.9b00333.

576   (45)   Mikhailov, E.; Vlasenko, S.; Niessner, R.; Poschl, U. Interaction of Aerosol Particles Composed
577   of Protein and Salts with Water Vapor: Hygroscopic Growth and Microstructural
578   Rearrangement. *Atmospheric Chemistry and Physics* **2004**, *4* (2), 323–350.

579   (46)   Stokes, R. H.; Robinson, R. A. Interactions in Aqueous Nonelectrolyte Solutions. I. Solute-
580   Solvent Equilibria. *The Journal of Physical Chemistry* **1966**, *70* (7), 2126–2131.
581   https://doi.org/10.1021/j100879a010.

582   (47)   Davies, J. M.; Viney, C. Water–Mucin Phases: Conditions for Mucus Liquid Crystallinity.
583   *Thermochimica Acta* **1998**, *315* (1), 39–49. https://doi.org/10.1016/S0040-6031(98)00275-5.

584   (48)   Dette, H. P.; Qi, M.; Schröder, D. C.; Godt, A.; Koop, T. Glass-Forming Properties of 3-
585   Methylbutane-1,2,3-Tricarboxylic Acid and Its Mixtures with Water and Pinonic Acid. *The*

586   *Journal of Physical Chemistry A* **2014**, *118* (34), 7024–7033.
587   https://doi.org/10.1021/jp505910w.

588 (49) Quinn, P. K.; Bates, T. S.; Schulz, K. S.; Coffman, D. J.; Frossard, A. A.; Russell, L. M.; Keene, W.
589   C.; Kieber, D. J. Contribution of Sea Surface Carbon Pool to Organic Matter Enrichment in Sea
590   Spray Aerosol. *Nature Geoscience* **2014**, *7*, 5.

591 (50) Zobrist, B.; Soonsin, V.; Luo, B. P.; Krieger, U. K.; Marcolli, C.; Peter, T.; Koop, T. Ultra-Slow
592   Water Diffusion in Aqueous Sucrose Glasses. *Physical Chemistry Chemical Physics* **2011**, *13*
593   (8), 3514. https://doi.org/10.1039/c0cp01273d.

594 (51) Bones, D. L.; Reid, J. P.; Lienhard, D. M.; Krieger, U. K. Comparing the Mechanism of Water
595   Condensation and Evaporation in Glassy Aerosol. *Proceedings of the National Academy of*
596   *Sciences* **2012**, *109* (29), 11613–11618. https://doi.org/10.1073/pnas.1200691109.

597 (52) Freedman, M. A. Phase Separation in Organic Aerosol. *Chemical Society Reviews* **2017**, *46*
598   (24), 7694–7705. https://doi.org/10.1039/C6CS00783J.

599 (53) Berkemeier, T.; Shiraiwa, M.; Pöschl, U.; Koop, T. Competition between Water Uptake and Ice
600   Nucleation by Glassy Organic Aerosol Particles. *Atmospheric Chemistry and Physics* **2014**, *14*
601   (22), 12513–12531. https://doi.org/10.5194/acp-14-12513-2014.

602 (54) Lu, J. W.; Rickards, A. M. J.; Walker, J. S.; Knox, K. J.; Miles, R. E. H.; Reid, J. P.; Signorell, R.
603   Timescales of Water Transport in Viscous Aerosol: Measurements on Sub-Micron Particles
604   and Dependence on Conditioning History. *Phys. Chem. Chem. Phys.* **2014**, *16* (21), 9819–9830.
605   https://doi.org/10.1039/C3CP54233E.

606 (55) Song, M.; Ham, S.; Andrews, R. J.; You, Y.; Bertram, A. K. Liquid–Liquid Phase Separation in
607   Organic Particles Containing One and Two Organic Species: Importance of the Average O:C.
608   *Atmos. Chem. Phys.* **2018**, *18* (16), 12075–12084. https://doi.org/10.5194/acp-18-12075-
609   2018.

610 (56) Song, M.; Marcolli, C.; Krieger, U. K.; Zuend, A.; Peter, T. Liquid-Liquid Phase Separation and
611   Morphology of Internally Mixed Dicarboxylic Acids/Ammonium Sulfate/Water Particles.
612   *Atmospheric Chemistry and Physics* **2012**, *12* (5), 2691–2712. https://doi.org/10.5194/acp-12-
613   2691-2012.

614 (57) Fard, M. M.; Krieger, U. K.; Peter, T. Kinetic Limitation to Inorganic Ion Diffusivity and to
615   Coalescence of Inorganic Inclusions in Viscous Liquid–Liquid Phase-Separated Particles. *J.*
616   *Phys. Chem. A* **2017**, *121* (48), 9284–9296. https://doi.org/10.1021/acs.jpca.7b05242.

617 (58) Ma, S.; Chen, Z.; Pang, S.; Zhang, Y. Observations on Hygroscopic Growth and Phase
618   Transitions of Mixed 1, 2, 6-Hexanetriol∕(NH4)2SO4 Particles: Investigation of the Liquid–
619   Liquid Phase Separation (LLPS) Dynamic Process and Mechanism and Secondary LLPS during
620   the Dehumidification. *Atmos. Chem. Phys.* **2021**, *21* (12), 9705–9717.
621   https://doi.org/10.5194/acp-21-9705-2021.

622 (59) Dette, H. P.; Koop, T. Glass Formation Processes in Mixed Inorganic/Organic Aerosol Particles.
623   *The Journal of Physical Chemistry A* **2015**, *119* (19), 4552–4561.
624   https://doi.org/10.1021/jp5106967.
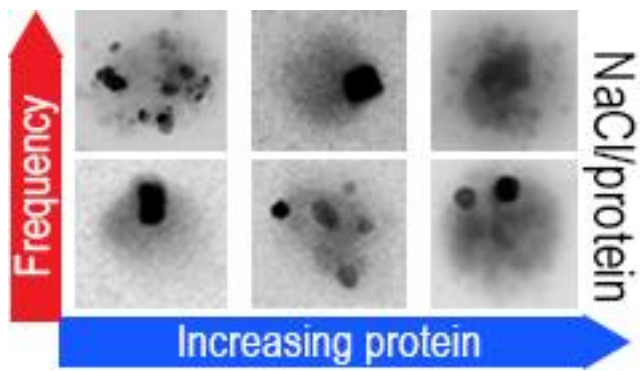
625

626

627

628

629

630

631

632

633

634

635

636   For Table of Contents Only

637